ASTRONOMY

Extreme energetic particle events by superflare-asssociated CMEs from solar-like stars

Junxiang Hu[1], Vladimir S. Airapetian[2,3]*, Gang Li[1], Gary Zank[1], Meng Jin[4,5]

Discovery of frequent superflares on active cool stars opened a new avenue in understanding the properties of eruptive events and their impact on exoplanetary environments. Solar data suggest that coronal mass ejections (CMEs) should be associated with superflares on active solar-like planet hosts and produce solar/stellar energetic particle (SEP/StEP) events. Here, we apply the 2D Particle Acceleration and Transport in the Heliosphere model to simulate the SEPs accelerated via CME-driven shocks from the Sun and young solar-like stars. We derive the scaling of SEP fluence and hardness of energy spectra with CME speed and associated flare energy. These results have crucial implications for the prebiotic chemistry and expected atmospheric biosignatures from young rocky exoplanets as well as the chemistry and isotopic composition of circumstellar disks around infant solar-like stars.

INTRODUCTION

The discovery of more than 4700 exoplanets in our Galaxy suggests that many exoplanetary systems contain close-in rocky exoplanets in the habitable zones around young magnetically active G, K, and M dwarfs (*1*). These exoplanets should be exposed to high-stellar coronal x-ray and extreme ultraviolet (UV) and wind mass fluxes. Observations in the optical band by Kepler, Transit Exoplanet Survey Satellite (TESS), and ground-based telescopes have revealed thousands of frequent superflares with energies ranging from 10^{33} up to 10^{35} ergs from hundreds of cool K-M planet-hosting dwarf stars, providing a mechanism by which host stars may have profound effects on the physical and chemical evolution of exoplanetary atmospheres (*2*–*6*). We will refer to solar and stellar flares with energies $\geq 10^{33}$ ergs as superflares. Intense solar and stellar flares are sources of x-ray and extreme UV emission and energetic particles accelerated at the coronal flare sites and referred to as impulsive solar energetic particles (SEPs) as they last for a few hours (*7*). In addition, large (>X5.5 class) solar flares are usually accompanied by ejection of fast (up to 3000 km/s) and massive (10^{16}g) coronal magnetized clouds referred to as coronal mass ejections or CMEs (*8*). As CMEs propagate out from the solar corona into interplanetary medium, they drive shocks. It is accepted that these shocks produce energetic protons and heavier ions at their fronts with energy more than 1 GeV that can last for a few days and are referred to as gradual SEP events (*9*, *10*).

Fast CME events can produce SEPs with hard energy spectra of particles that penetrate into Earth's atmosphere forming ground-level enhancement (GLE) events (*11*). Since the 1940s, more than 70 GLE events with good magnetic connection to large solar flares have been detected and characterized (see https:/gle.oulu.fi). Among them, the GLE event that occurred on 23 February 1956 had the hardest energy spectra, which was associated with a fast CME and a strong X (5 to 15) class flare with the estimated energy of 10^{32} to 5×10^{32} ergs (*12*). The Carrington event was estimated to be associated with an X45 class flare with the radiative energy of 5×10^{32} ergs. It was accompanied by the fast CME event propagating at 2360 km/s and caused the largest geomagnetic storm on record, but no signatures of a hard-spectrum SEP required for a GLE event was detected (*13*).

Our Sun historically produced a number of large flare events with energies more than 10^{33} ergs that we will refer to as solar superflares. These include eight possible superflare events that occurred in 7176, 5410, 5259, and 660 BCE and 775, 993, 1052, and 1279 CE (*14*–*16*). The fluence of these SEP events were so exceptionally high that they produced detectable amounts of ^{14}C in tree rings and a 300% increase in ^{10}Be in ice cores (for 775 CE) (*16*–*18*). In comparison, the energetic protons from the SEP event of 23 February 1956 initiated the increase of the production rate of ^{10}Be to a rate of 5% (*19*). This and other studies suggest that the 775 CE SEP event was associated with a solar X285 ± X140 class superflare and an associated CME with the energy of 2×10^{33} ergs (*12*).

Unlike our current Sun, young (the first 0.7 Ga) solar analogs (G-type main sequence stars) are magnetically active stars (*5*, *20*). Their magnetic activity is manifested in the presence of strong surface magnetic fields up to a few hundred Gauss, large starspots covering up to 10% of a stellar surface, dense and hot bright x-ray corona, massive fast winds, and frequent flare activity (*5*, *20*–*23*). A substantial fraction of these stars (including F-, G-, K-, and M-type stars) show superflare events. From the strong correlation between the X-type solar flares and associated energetic CMEs, it is conceivable that energetic stellar CMEs should be associated with stellar superflares. Recent observations provided strong evidence for stellar CME events associated with superflares from K-M dwarfs (*24*). Theoretical models suggest that stellar superflares can be associated with energetic confined CMEs forming within active regions and halo-type CMEs driven by global-scale energizing shearing flows from young solar-like stars (*25*, *26*).

As in the case of solar CMEs, particles can be accelerated to very high energies at the front of CME-driven shock waves. It has been generally accepted that energetic particles in these events are accelerated via the diffusive shock acceleration (DSA). The DSA, also known as the first-order Fermi acceleration, was first proposed to explain the acceleration of galactic cosmic rays at supernova shocks [reviewed by (*27*)] and later applied to describe SEP acceleration at CME-driven shocks. Particles from gradual SEP events can amplify Alfvèn waves via wave-particle interactions, which also affects their subsequent transport through turbulent solar/stellar wind (*9*, *28*).

[1]Department of Space Science and CSPAR, University of Alabama in Huntsville, Huntsville, AL, USA. [2]NASA Goddard Space Flight Center/SEEC, Greenbelt, MD, USA. [3]American University, DC, USA. [4]SETI Institute, Mountain View, CA, USA. [5]Lockheed Martin Solar and Astrophysics Laboratory, Palo Alto, CA, USA.
*Corresponding author. Email: vladimir.airapetian@nasa.gov

The accelerated particles are a major source of ionization in circumstellar disks and (exo)planetary atmospheres around magnetically active stars as an important component of exoplanetary or astrospheric space weather, a subject that has emerged as an important subfield of exoplanetary science and which has a crucial influence upon factors of habitability (*5*). However, energy spectra of StEP events have not been modeled comprehensively.

Here, we expand our previous models of solar and stellar energetic particle events (*29*, *30*) and apply the two-dimensional (2D) improved Particle Acceleration and Transport in the Heliosphere (iPATH) model to model the SEP/StEP events driven by fast CMEs with energies corresponding to stellar superflares (10^{33} to 10^{35} ergs) observed in young solar-like stars. The iPATH model was developed by Zank *et al.* (*9*), who adopted an onion shell model of the CME-driven shock complex to obtain the source of energetic particles at the shock front. The model was updated by Rice *et al.* (*28*) who considered shocks with arbitrary strength and by Li *et al.* (*31*) who extended the original 1D PATH model by adding a transport module investigating particle propagation in the solar wind using a Monte-Carlo approach. Later, Li (*32*) extended the model to include energetic heavy ions. Explicit inclusion of shock obliquity was considered in (*33*) so that a better determination of the maximum energy at the shock front can be obtained. However, in the work of Li *et al.* (*33*), the shock obliquity was treated as a free parameter instead of a dynamic variable. Proper treatment of the shock obliquity was done in the 2D iPATH model (*34*), which tracks the evolution of the shock front and has the capability of simultaneously simulating energetic particle time intensity profiles and spectra at different locations. This is important for understanding observations made at multiple spacecraft of the same event [e.g., (*35*, *36*)]. Early applications of the 1D PATH code on individual SEP events have been pursued by Verkhoglyadova *et al.* (*37*, *38*). Recently, the 2D iPATH code has been successfully used to reproduce the time profiles and event fluences for two large GLE events (*39*, *40*). These studies show the applicability of using the iPATH code and its capabilities to model extreme SEP and StEP events as pursued in this work.

RESULTS

Here, we present the simulation results of SEP/StEP events driven by CMEs with different energies launched during superflares from solar-like (G-K type) stars. We model the acceleration and transport of extreme SEP/StEP from the CME-driven shocks and obtain the proton fluence spectra at 1-AU (Astronomical Unit) observer locations. We then analyzed corresponding spectral characteristics in these large gradual SEP/StEP events.

First, we calculated the background solar/stellar wind environments using a 2D magnetohydrodynamic model for solar-like stars at different phases of evolution. Table 1 shows the input stellar wind parameters at 1 AU for three different stellar environments. Model 1 (m1) represents the typical parameters of our current solar wind environments as a reference model. The m2 and m3 are set to describe young solar-like (G-type) stars at ages of 0.3 and 0.7 Ga, respectively, with shorter rotation periods, denser stellar winds, and stronger magnetic fields as compared to the current Sun. The stellar wind parameters for m2 and m3 are based on results from (*23*).

We then inject CMEs from the inner boundary at 0.05 AU ($\sim 10 R_\odot$) in each stellar wind setup. Figure 1 is a snapshot of the CME-driven shock for each scenario at t = 12 hours from the magnetohydrodynamic (MHD) module, where the initial CME speed is set to be 3000 km/s specified as an extreme event in the heliospheric environment (*41*). Figure 1 shows the global stellar magnetic field geometries (black spiral lines) for the cases with rotation periods of 25.3 days for m1, 10 days for m2, and 5 days for m3.

For each of the stellar wind models, we follow the subsequent transport of the accelerated particles from the shock to an observer at 1 AU (shown as the white dots in Fig. 1). Three observer longitudes, at −10°, −70°, and −130° with respect to the CME center for m1, m2, and m3 scenarios, respectively, are chosen to ensure that the observers are connected to a similar longitude at the inner boundary through magnetic field lines at the beginning of the simulation. We inject CMEs with four different speeds for each stellar wind model, including the mentioned 3000 km/s case across all three models. For m1, we also include 1500-, 2000-, and 2500-km/s cases to cover the often observed CME speed in our heliosphere. For m2 and m3 scenarios, we added CMEs propagating at 4500, 6000, and 7500 km/s to investigate the extreme events from young solar-like stars. The iPATH model provides the time-intensity profile for a wide range of energies at the observer locations as output. We then integrate the time-intensity profile over the duration of the events to obtain the event-integrated fluence.

Figure 2A shows the simulated event-integrated spectra at 1 AU for these cases. For each of the cases, we first obtain the time-intensity result for a wide range of energies. Figure 2B shows the time-intensity profile of five different energies for the m3 scenario, 3000 km/s CME case as an example. The x axis specifies the time from flare onset. We integrate the intensities over the duration of the event to get the event-integrated spectra in Fig. 2A. Similar to observations, the bulk of our simulated spectra exhibits a double power-law shape. We fit the event-integrated spectra from these scenarios with the double power-law spectrum in the form similar to (*42*)

$$\frac{dJ}{dE} = A\left(\frac{E}{E_b}\right)^{-\gamma_1}\left[1+\left(\frac{E}{E_b}\right)^2\right]^{\frac{\gamma_1-\gamma_2}{2}} \quad (1)$$

where γ_1 and γ_2 are the spectral indices for protons with energies lower and higher than the spectral break energy E_b, respectively. Examples of the fits are shown in Fig. 2C.

Table 1. Stellar wind parameters for each case at 1 AU.

Case	Stellar age (Ga)	Rotation period (days)	Proton density (cm^{-3})	Wind speed (km/s)	Magnetic field (nT)
m1	4.6	25.3	5	400	5
m2	0.7	10	50	500	20
m3	0.3	5	500	700	50

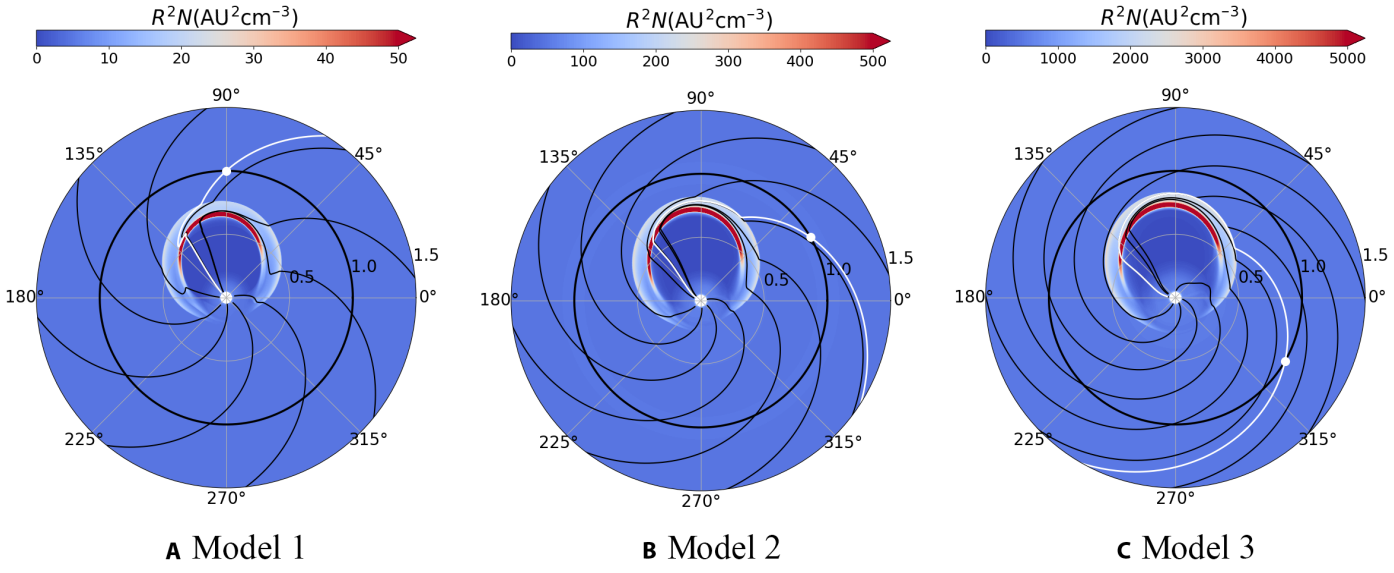

Fig. 1. Global magnetic field and configuration for CME-driven shocks from MHD simulations. The stellar rotation periods are 25.3 days for m1 (**A**), 10 days for m2 (**B**), and 5 days for m3 (**C**). The initial CME speed is 3000 km/s in all three scenarios. The CMEs are centered at 100° and the observers (white dots) are set at 90°, 30°, and 330° for m1, m2, and m3, respectively at 1 AU. These snapshots are taken at 12 hours after the CME initiation from the MHD simulation.

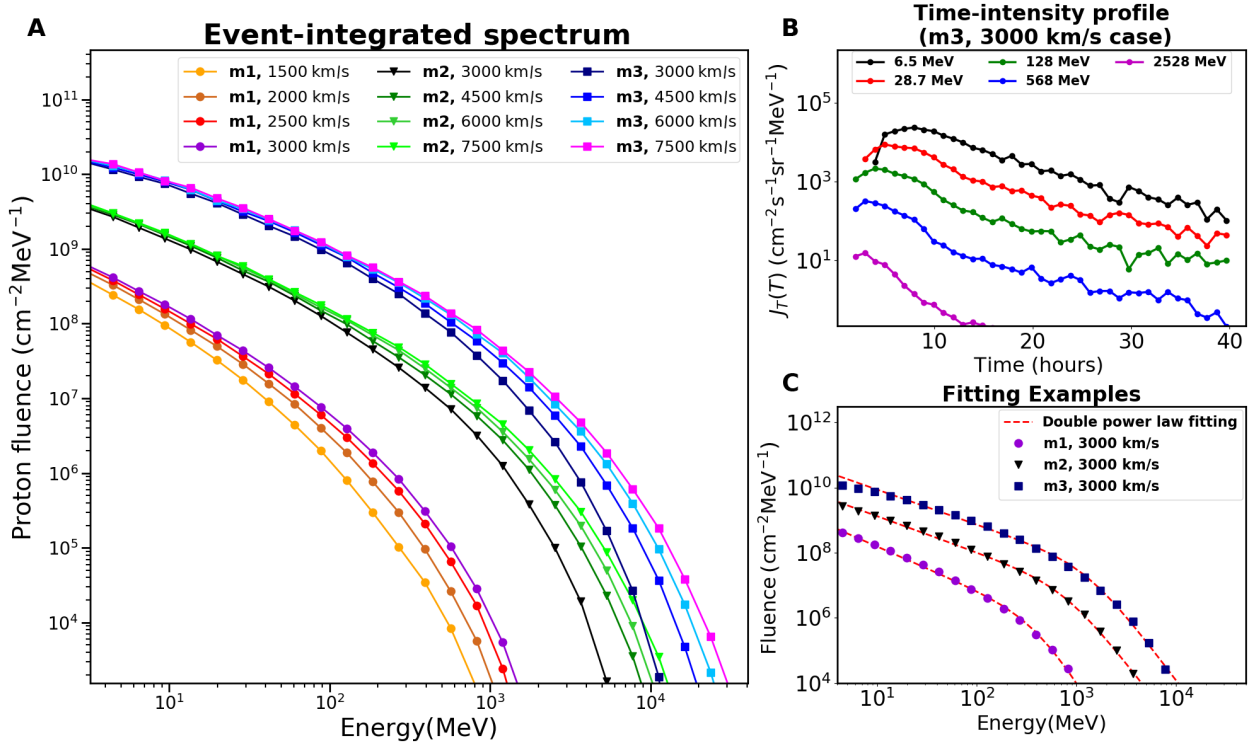

Fig. 2. The solar and stellar energetic particle fluences and fluxes from 2D iPATH simulations. (**A**) Event-integrated energy spectra of SEP/StEP driven by CMEs with various speeds for m1, m2, and m3 scenarios at the corresponding 1 AU observer locations. (**B**) Time-intensity profile for the 3000 km/s CME case of m3 scenario. (**C**) Double power-law fitting for the CME propagating at 3000 km/s in m1, m2, and m3 scenarios.

To relate the results of our simulations for m1, m2, and m3 with observations, we will use the statistical relation between the peak Geostationary Operational Environmental Satellites (GOES) 1- to 8-Å Soft X ray (SXR) flux, F_{SXR}, and the flare bolometric energy, E_{bol}, to estimate the peak SXR flux in each case. It is suggested in a number of solar flare studies (*43*, *44*) that this correlation can be written in a dimensionless form as follows

$$\frac{E_{\mathrm{bol}}}{10^{30}\,\mathrm{erg}} \approx \left(\frac{F_{\mathrm{SXR}}}{2.0\times 1\,0^{-6}\,\mathrm{W\,m^{-2}}}\right)^{0.78} \quad (2)$$

This power-law index is close to the one obtained by (*45*) for solar and stellar flares that varies between 0.84 ±0.04 and 1.18 ±0.04, which depends on the fitting method. With this uncertainty in

mind, we will assume that the bolometric flare energy is proportional to the SXR peak flux as described in Eq. 2.

We follow (*44*) in assuming that the CME energy is equal to the total radiated energy released in a flare: $E_{bol} \approx E_{CME}$. Thus, we can estimate the SXR peak flux of our simulated extreme events from CME energies

$$F_{SXR} \approx 7.3 \times 10^{-4} \left(\frac{E_{CME}}{10^{32}\,\mathrm{erg}} \right)^{1.28} \left(\mathrm{W\,m^{-2}}\right) \quad (3)$$

According to statistical studies reported in (*44*), most of the CME total energy is in the form of its kinetic energy. To estimate the CME energies for all the cases, we first calculate the CME kinetic energy for the 3000 km/s case in m1 scenario with the appropriate model input parameters. The mass of the injected CME plasma blob is calculated by multiplying the density input with the volume estimated from CME width and duration input. We obtain an energy estimation of 5×10^{32} ergs and a corresponding F_{SXR} estimation of 0.0057 W/m^2 (an X57 flare) for this case. We then use the dependence of $E_{cme} \propto M_{cme} V_{cme}^2$ to estimate the CME energies and F_{SXR} for all other cases.

Table 2 shows the detailed SEP/StEP characteristics for all 12 simulated scenarios. Columns 3 through 5 present the spectral break energy, E_b in MeV and the fitted spectral indices using Eq. 1, γ_1 and γ_2, respectively. Figure 2 shows that all simulated SEP events have the prebreak spectral index within the range of $\gamma_1 \in$ (1.0, 1.4). The postbreak spectral index varies slightly with the CME speed, with $\gamma_2 \in$ (3.6, 5.3). Columns 6 and 7 show the 1-AU peak proton integral flux [in proton flux unit (pfu) or cm^2 s^{-1} sr^{-1}] integrated over energies >10 MeV and the proton integral fluence (in cm^{-2}) from the event-integrated spectra at energies >430 MeV (~1 GV rigidity), respectively. These fluences will be compared with recent GLE observations. The last two columns of Table 2 present the estimated CME energies (in ergs) and the corresponding flare peak SXR fluxes calculated from Eq. 3. We present the SXR peak flux in terms of flare classes. An X1 flare corresponds to a 1- to 8-Å SXR peak flux of 10^{-4} Wm^{-2}. The SXR peak flux value in each case is the number after *X* times 10^{-4} Wm^{-2}.

In Fig. 2, the differential fluence at lower energies, which represent the majority of the total SEP/StEP fluences (cm^{-2}), scales roughly proportional to the background stellar wind density. For instance, the 10-MeV proton fluence for the 3000 km/scases in m1, m2, and m3 are 1.5×10^8, 1.3×10^9, and 8.6×10^9 (cm^{-2} MeV^{-1}), respectively, while the stellar wind density is increased 10-fold from m1 to m2 and from m2 to m3. This dependence is expected as the shock upstream density directly determines how many particles are injected into the DSA process. However, the enhancement is much more significant for the higher-energy proton fluences due to the shifted spectral break location. For instance, the 1-GeV proton fluence increases almost 200 times from m1 to m2.

Our model results provide direct comparison with the scaling relation between the peak proton integrated flux F_p (in pfu) and F_{SXR} of an associated flare event, which was derived analytically in (*46*) from simple scaling assumptions of magnetically driven eruptive events. Figure 3 shows the F_p (>10 MeV) versus F_{SXR} scatterplot for our model results (green markers) and a selection of observed SEP events (black circles) between 1997 and 2017 listed in Coordinated Data Analysis Workshops (CDAW) (see http://cdaw.gsfc.nasa.gov/CME_list/sepe/), similar to the last figure in (*46*). As it follows from columns 6 and 9 of Table 2, the relationship between the peak particle flux > 10 MeV and the peak SXR flux from the least squares fit (green dashed line) of our simulation results is $\underline{Fp}$ (>10 MeV) $\propto F_{SXR}^{0.771}$, which is close to the power-law index 5/6 derived in (*46*). In addition, the simulated peak proton fluxes, F_p (>10 MeV), are about two orders of magnitude lower than the upper bound for the corresponding fluxes estimated in (*46*). The close similarity in these power-law indices suggests that the F_p (>10 MeV) − F_{SXR} scaling derived from SEP events can be applied to StEP events. This can be understood because the observed spectral break energies in major SEPs are usually greater than 10 MeV (*47*).

The fitted spectral break energy, E_b, has a positive correlation with both stellar wind density and CME speed and increases by more than one order of magnitude from m1 to m3 scenarios. This can be understood as a result of greater Alfvén wave energy

Table 2. SEP characteristics from simulation results.

Model	V_{CME} (km/s)	E_b (MeV)	γ_1	γ_2	>10 MeV peak flux (pfu)	>430 MeV fluence (cm^{-2})	*E_{CME} (erg)	†Flare class
m1	1500	125	1.40	3.80	1.86×10^3	2.67×10^6	1.3×10^{32}	X9.7
	2000	249	1.37	4.63	2.76×10^3	9.23×10^6	2.2×10^{32}	X20
	2500	271	1.31	4.23	3.92×10^3	2.45×10^7	3.5×10^{32}	X36
	3000	453	1.35	5.23	4.71×10^3	4.09×10^7	5.0×10^{32}	X57
m2	3000	791	1.11	3.96	1.13×10^5	4.18×10^9	5.0×10^{33}	X1100
	4500	1064	1.09	3.60	1.87×10^5	8.16×10^9	1.1×10^{34}	X3100
	6000	1362	1.07	3.76	2.61×10^5	1.07×10^{10}	2.0×10^{34}	X6400
	7500	1749	1.07	3.90	3.15×10^5	1.30×10^{10}	3.1×10^{34}	X11,000
m3	3000	1332	1.07	4.07	1.04×10^6	5.35×10^{10}	5.0×10^{34}	X21,000
	4500	1571	1.04	3.53	1.58×10^6	8.92×10^{10}	1.1×10^{35}	X58,000
	6000	2065	1.03	3.60	2.03×10^6	1.19×10^{11}	2.0×10^{35}	X120,000
	7500	2824	1.05	3.77	2.48×10^6	1.36×10^{11}	3.1×10^{35}	X220,000

*CME energy scaled based on CME speed and mass. †Flare classes based on 1- to 8-Å˚ SXR peak flux. An X1 flare corresponds to a peak flux of 10^{-4} Wm^2. The number after X specifies how many times stronger the peak SXR flux is than X1.

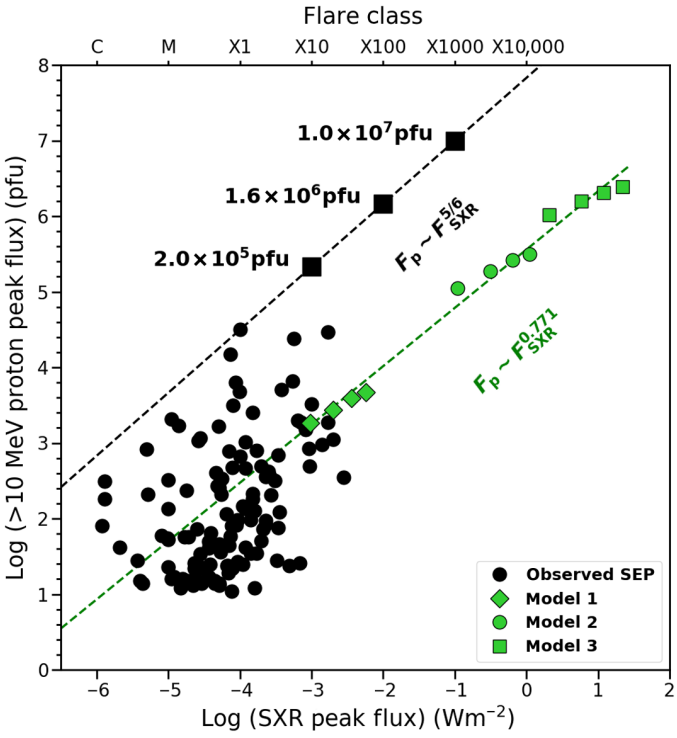

Fig. 3. F_p (>10 MeV) versus F_{SXR} scaling relation for solar and stellar events. The black filled circles are major SEPs between 1997 and 2017. Green markers are simulation results for m1 (diamonds), m2 (circles), and m3 (squares). The black dashed line is the estimated upper limit of F_p given by (*46*), with black squares being the upper limits for X10, X100, and X1000 class flares. The green dashed line is the least squares fit of the 12 simulated cases.

flux at the shock, excited by streaming protons, associated with higher shock speed and upstream stellar wind density. In addition, a higher CME speed means that particles will gain more energy during each shock crossing in the DSA process. The maximum energy E_{max} of accelerated protons in the simulations, which is also the cutoff energy of the event-integrated spectrum for each case, scales almost linearly with CME speed as a consequence of the DSA acceleration mechanism. Note that the shock formation in our simulation occurs at a height above 0.1 AU after the CME injection. As a result, the CME shock acceleration that occurrs at earlier times (or lower coronal heights) is not included in our model. We will discuss more realistic SEP models driven by CME shocks that occur at lower heights in the forthcoming paper.

To demonstrate how well our simulated scaling relations fit with the scaling from recently observed GLE events in the current solar environment, we plot the F_{SXR} versus >200 MeV proton integral fluence of the simulated SEP/StEP events on top of the scatterplot from (*12*) in Fig. 4A. The black square markers represent the data from the solar GLEs occurred between the year 1976 and 2012, with the >200 and >430 MeV fluences derived from the spectral parameters of GLEs provided in (*48*). Koldobskiy *et al.* (*49*) have recently revisited the spectral fitting for these GLEs based on a modified Band function spectral shape. While the fluences at high energies (>430 Mev) differ for a few individual events by a factor of 2 to 6, the fitting slope does not change significantly, and thus, the GLE scaling results in (*12*) remain consistent with the updated fluences. Thus, in this work, we directly compare our simulated fluences with the analyses in (*12*). The solid line is a reduced major axis fit from these GLE events, with a dispersion given by the dashed lines. Blue and red circles indicate the possible data point positions for the 1956 and 774 events on the fit lines based on their >200 MeV fluences values, as shown in (*12*). The scatter in GLE fluence data can be attributed due to different magnetic connectivity between the observer and the CME nose and uncertainties in SXR peak flux measurements. The green markers are our simulated scenarios for m1 (diamond), m2 (circle), and m3 (square). Similarly, Fig. 4B presents the scatterplot of the SEP/StEP fluence at >200 versus >430 MeV reported in (*12*), with our simulated fluences from superflare-associated SEP/StEP events added as the green markers.

Figure 4A shows that the energetic particle fluence at energies >200 MeV in the m1 and m2 models for the 3000 km/s CME speed scenario lies close to the upper boundary of the fit line, because we put the observer at a longitudinal location with optimal magnetic connection with the CME center. However, the corresponding StEP fluences derived from m3 and m2 models in higher CME speed scenarios are located significantly lower than the upper limit despite having a similar magnetic connection. We interpret this as a result of the double power-law shape of the event-integrated spectra. We can gather from Fig. 2 and Table 2 that the spectral break energies for the extreme cases in m2 and m3 are well above 200 MeV—the lower energy limit for this integral fluence. In these extreme StEP cases, the time-integrated fluence scales with the area under a harder prebreak spectrum with a power index of ~ −1.2 rather than the area under a softer postbreak spectrum with a power index of ~ −4. In much stronger stellar energetic particle events, one should expect a slower increase of >200 MeV fluence with the SXR peak flux.

For the m1 model scenario with four specified cases of CME speeds (1500 to 3000 km/s), the four data points are roughly parallel to the black fit line, suggesting our simulation results for the solar wind environment agree well with the observations. For m2 and m3 scenarios with much faster CME speed (3000 to 7500 km/s), the trend starts to flatten as the CME speed increases. This is because the shock compression ratio and the wave intensity at the shock front in the iPATH model depend on the shock speed in a nonlinear way.

This is the first theoretical study to date that simulates SEP/StEP energy spectra from high energy and fast CMEs, and more detailed analysis will follow in the forthcoming papers. In addition, note that the SXR peak flux is estimated from the empirical correlation in Eq. 2. However, it is unclear whether this correlation holds for these ultrafast CMEs.

In the original scatterplot in Fig. 4B, Cliver *et al.* (*12*) also added the 1956 GLE event fluences from (*48*) and the 774 and 993 AD event fluences from (*17*). These three additional extreme event data points were compared with the ordinary least square fit, $y = 0.913x - 0.452$ (black line), from the 1976–2012 GLEs, and found to be about one order of magnitude above the fit line. It was suggested that a harder than usual proton spectrum is required for this offset. However, these three events fall well on an ordinary least squares fit to the simulated events in this work, which yields $y = 1.172x - 2.127$ (green dashed line). For the same reason as the extreme SEP events have spectral break energies over 430 MeV, the 200- to 430-MeV energy range falls in the harder prebreak spectrum. While for the often observed GLEs, where the spectral break energies are usually tens of MeV (*47*), the 200- to 430-MeV energy

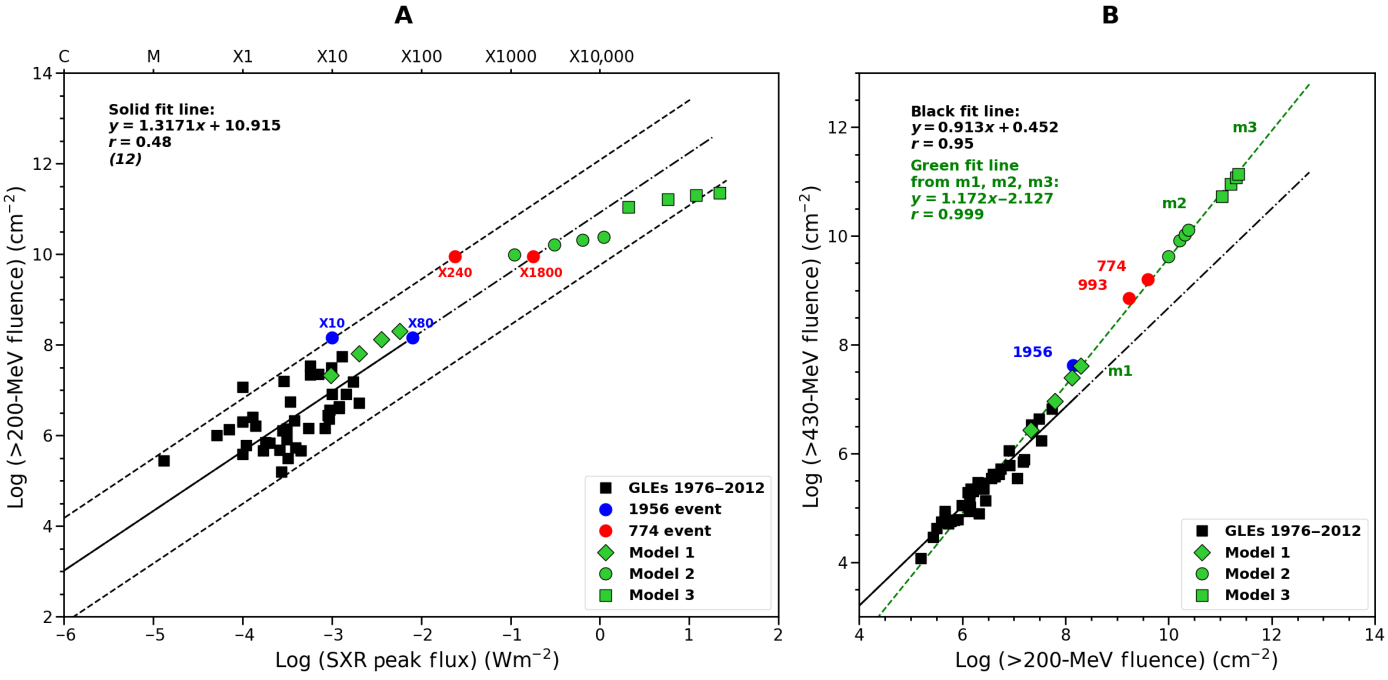

Fig. 4. Scaling relations between *F* (>200 MeV) versus F_{SXR} and *F* (>430 MeV) versus *F* (>200 MeV) for solar and stellar events. (**A**) Scatterplot of the log of the >200-MeV proton fluence of SEP/StEPs versus the log of F_{SXR} of associated (super)flares. Black squares represent GLE events that occurred 1976–2012, blue and red circles describe 1956 and 775 AD GLE events, respectively; the green diamonds, squares, and cubes represent SEP/StEP events for m1, m2, and m3 model scenarios, respectively. (**B**) Scatterplot of the log of the >430-MeV proton fluence versus the log of the >200-MeV fluence for solar GLEs; 1956, 775, and 993 GLE events; and simulated SEP/StEP events. The black solid line represents an ordinary least square fit to the recent observed GLE events in (*12*). Our m2 and m3 model spectra show the energy spectra of StEPs specified by the green dashed fit line to be harder than that derived from the extrapolation from the solar GLE events shown by the black dashed-dotted fit line).

range falls into the softer postbreak spectrum. One must take this into consideration when estimating the high-energy fluence for a stellar energetic proton event and not to use predicted values based on observed solar events. It would otherwise be a severe underestimation for the ultra high energy proton fluences, which is of great importance for exoplanetary studies.

DISCUSSION

We report the results of numerical simulations of extreme SEP/StEP events to examine the impact of stellar superflare–associated extreme CME events on the properties of gradual stellar energetic particles events using the 2D iPATH model. We developed and modeled 12 scenarios of SEP/StEP events associated with CME energies ranging from 10^{32} to 10^{35} erg, which are associated with superflares from the current and the young (the first 0.7 Ga) Sun and magnetically active solar-like (G- and K-type) stars. We derived the time history, fluence spectra, and maximum particle energies for all these scenarios. Our major findings from the simulated scenarios can be summarized as follows:

1) A CME-driven shock propagating at a fixed speed in the higher wind density and stronger and more twisted magnetic field environment characteristic of younger rapidly rotating solar-like stars produces much stronger (high fluence) and harder-spectra StEP events. The lower-energy (<100 MeV) proton fluence scales proportionally to the wind density, while higher-energy (>100 MeV) proton fluence acquires greater enhancement due to the harder spectral shape.

2) A faster CME-driven shock produces the SEP event with greater maximum proton energy (with nearly linear correlation) and the higher spectral break energy in SEP events, contributing to a harder proton spectrum at higher energies.

3) The energy spectra in extreme stellar events associated with superflares are harder (indicated by the >430 MeV to >200 MeV fluence ratio) than that observed in large SEPs from the current Sun.

This suggests that empirical correlations between solar SXR peak flux and SEP fluence at higher energies cannot be extrapolated for extreme StEP events (*50*–*52*). Thus, realistic estimates of extreme StEP fluences should only be derived from physics-based models that specify a data-constrained stellar wind environment (*23*). In addition, we conclude that the fluence depends on the density of stellar winds of active stars producing CME events. This result has direct implications for fluences of young superflare producing G and K dwarfs with rotation periods less than 10 days (*21*). A recent study by Airapetian *et al.* (*23*) modeled the stellar corona of one such star, κ^1 Ceti, resembling the environment of the early Earth at the time when life arose on our planet. Specifically, they have shown that the higher wind density and velocity difference between fast and slow wind components of this star can drive shocks in the stream interaction regions, providing greater and more highly energized seed particle populations that will enhance SEP production by CME-driven shocks.

The derived high-fluence hard-spectra StEP events (m2 and m3 model scenarios) can also play a crucial role in the chemical models of close-in gas giants and prebiotic chemistry of rocky exoplanets around young G, K, and M dwarfs that generate superflare events

including K2-18b, AU Mic b, and other systems. We would therefore expect the irradiation of their atmospheres with associated CMEs that would interact and compress exoplanetary magnetospheres opening up their polar regions to low latitudes as discussed in (*53*). The associated hard-spectra StEPs with energies >430 MeV (the rigidity greater than 1 GV) would then efficiently penetrate into the lower layers of exoplanetary atmospheres (at the atmospheric pressure ≤ 1 bar), induce ionization of atmospheric species via collisions, and ignite chemical changes via collisional dissociation and excitation (*5*, *54*–*56*). Recent theoretical and experimental studies show that as energetic particles penetrate into a N_2-CO_2–rich atmosphere of a rocky exoplanet with a trace amounts of methane and water vapor, they ignite the formation of complex molecules including nitrous oxide, hydrogen cyanide, formaldehyde, the precursors of proteins, complex sugars, and building blocks of nucleobases (*5*, *53*, *57*–*60*).

Our results also have important implications for the habitability conditions on rocky exoplanets around M dwarfs including TRAPPIST-1 and Proxima b. It is known that M dwarfs retain a high level of magnetic activity in terms of production of frequent and large flares with energies up to 10^{33} ergs for billions of years (*61*) and thus are expected to generate fast CME events resulting in production of high-fluence StEPs similar to those described by the m2 model. Because exoplanets in close-in habitable zones around M dwarfs are tidally locked, they are expected to have weak magnetic moments. Weaker magnetospheres of close-in exoplanets will be compressed due to the dynamic pressure of dense stellar winds and CMEs and thus would not be protected from penetration of StEPs by an extended magnetosphere. If fluence of hard-spectrum StEP is high, then the surface fluxes of ionizing radiation can reach lethal doses for living organisms and thus sterilize surface life on habitable exoplanets [e.g., (*4*, *62*)]. Thus, the detailed understanding of properties of extreme SEP/StEP events and their impact on the (exo)planetary atmospheric chemistry, climate, and induced atmospheric and surface particle radiation field is crucial in assessing habitability conditions and atmospheric biosignatures to be performed with the upcoming missions including those of the James Webb Space Telescope.

The organic chemistry and lifetime of circumstellar disks are also affected by the magnetic activity from G and K pre-main sequence (≤ 10 Ma) host stars. These stars produce frequent super and mega-flares (up to the energy of 10^{38} ergs) and thus are associated with SEP accelerated energetic protons with the maximum energy of 50 GeV that are capable of penetrating the equatorial regions of the disk and igniting enhanced ionization via collisions with disk species [see for example, (*63*)]. The recent simulations suggest that such high-ionization regions can be produced by high-fluence SEPs required to explain high ratios of HCO^+ to N_2H^+ observed in disks around young stars with Atacama Large Millimeter/submillimeter Array (ALMA) (*64*). Our results can also play a critical role in understanding the chemistry and isotopic composition of our own early solar system and other protoplanetary systems.

MATERIALS AND METHODS

To simulate the acceleration and transport processes in large gradual shock-driven SEP events initiated by fast CME events associated with superflares from active solar-like stars, we apply the 2D iPATH model that includes three modules: (i) a 2D MHD model of the stellar wind and CME-driven shock in the ecliptic plane using an updated version of ZEUS-3D MHD (v3.6) code (*65*); (ii) a shell module that follows the acceleration of particles at the shock front and their subsequent convection and diffusion downstream of the shock. The downstream of the shock is separated into concentric shells where the injection energy, maximum energy, and distribution functions of particles are tracked. Each shell is generated behind the shock front every certain time steps and divided longitudinally into parcels with a 5° width. In this module, we also calculate the escaped particle spectra at a distance ahead of the shock; (iii) a transport module that models the transport of SEPs in the interplanetary medium that uses escaped particle spectra. This model is based on the focused transport equation modified with a cross-field diffusion term, which is solved using a backward stochastic differential equation method.

The model input includes the stellar wind, CME, and turbulence parameters. The iPATH model outputs time-intensity profiles of energetic particles at desired observer locations for the entire duration of SEP/StEP events. A steady background stellar wind environment in a polar coordinate system (radial, *r*, and helio longitude) with the background interplanetary magnetic field is described by a Parker spiral

$$B_r = B_0\left(\frac{R_0}{r}\right)^2; B_\phi = B_r\left(\frac{\Omega r}{u_{sw}}\right)(r \gg R_0) \quad (4)$$

We set the simulation domain to be from the outer solar corona at 0.05 to inner (helio) astrosphere at 3 AU on a 2D 2000 × 360 grid (radial × longitudinal dimensions) in the ecliptic plane for models m1, m2, and m3 described in Table 1 (see Results). To simulate a CME-driven shock structure, we perturb the stellar wind parameters at the inner boundary (0.05 AU, $\sim 10R_\odot$) centering at $\phi_c = 100°$ with an opening angle of 120°. At the center location ϕ_c, the solar wind number density and temperature are increased by factors of 4 and 1.33 from the ambient values, respectively, with a 1-hour duration. The magnetic field is not perturbed at the inner boundary as we merely inject a hydrodynamic CME structure to obtain the shock information. Gaussian distribution with a variance $\sigma = 66.6°$ is used to characterize the variation of perturbation in longitude.

To follow the acceleration of particles at the shock complex, shock parameters, including shock oblique angle θ_{BN} (the angle between shock normal direction and upstream magnetic field lines), compression ratio, and shock speed, are extracted from the MHD simulation along the shock front. The total diffusion coefficient κ is computed through

$$\kappa = \kappa_\parallel \cos^2\theta_{BN} + \kappa_\perp \sin^2\theta_{BN} \quad (5)$$

where $\kappa_\parallel$ and $\kappa_\perp$ are the parallel and perpendicular diffusion coefficient, respectively. The diffusion coefficient κ describes how efficiently the particles are confined near the shock and, thus, affects the particle acceleration rate and governs the maximum energy that particles can reach through the DSA mechanism. The suprathermal seed population upstream of the shock is set to follow a single power-law distribution with a spectral index of −3.5. The injection efficiency, which is the ratio of the particle flux that participates the acceleration to the total injected particle flux, is set to be a fixed number of 0.5%. The turbulence level $\delta b^2/B_0^2$ at 1 AU is set to be 0.5, with a radial dependence of $\delta b^2 \sim r^{-3.5}$. Details on the choices of these parameters can be found in our previous work (*29*, *34*). The

acceleration module calculates the escaped energetic particles' distribution functions along the shock throughout the shock's propagation. These distribution functions at different times and locations are used as the moving source of energetic particles for the subsequent transport module.

Perpendicular diffusion plays an important role in particle acceleration at quasi-perpendicular (large θ_{BN}) shocks, which often emerge in a typical tight Parker spiral geometry of rapidly rotating young stars (*30*). Once accelerated particles escape from the shock complex, we follow their propagation in the solar/stellar wind described by a modified focused transport equation. While charged particles tend to move along individual field lines, they may also experience perpendicular diffusion due to the actual crossing of field lines via scattering or drift and random walking along meandering field lines. Note that the geometry of the spiral field line determines whether the perpendicular diffusion is in the azimuthal or radial direction. In Fig. 1, we can see that m3 has a much tighter field line spiral than m1, which represents our current Sun. Thus, in the m3 case, particles are mainly accelerated at a quasi-perpendicular shock and the perpendicular diffusion in the transport process has a much larger radial component. Whereas in the m1 case, the perpendicular diffusion mainly contributes to the longitudinal transport.

REFERENCES AND NOTES

1. S. Bryson, M. Kunimoto, R. K. Kopparapu, J. L. Coughlin, W. J. Borucki, D. Koch, V. S. Aguirre, C. Allen, G. Barentsen, N. M. Batalha, T. Berger, A. Boss, L. A. Buchhave, C. J. Burke, D. A. Caldwell, J. R. Campbell, J. Catanzarite, H. Chandrasekaran, W. J. Chaplin, J. L. Christiansen, J. Christensen-Dalsgaard, D. R. Ciardi, B. D. Clarke, W. D. Cochran, J. L. Dotson, L. R. Doyle, E. S. Duarte, E. W. Dunham, A. K. Dupree, M. Endl, J. L. Fanson, E. B. Ford, M. Fujieh, T. N. Gautier III, J. C. Geary, R. L. Gilliland, F. R. Girouard, A. Gould, M. R. Haas, C. E. Henze, M. J. Holman, A. W. Howard, S. B. Howell, D. Huber, R. C. Hunter, J. M. Jenkins, H. Kjeldsen, J. Kolodziejczak, K. Larson, D. W. Latham, J. Li, S. Mathur, S. Meibom, C. Middour, R. L. Morris, T. D. Morton, F. Mullally, S. E. Mullally, D. Pletcher, A. Prsa, S. N. Quinn, E. V. Quintana, D. Ragozzine, S. V. Ramirez, D. T. Sanderfer, D. Sasselov, S. E. Seader, M. Shabram, A. Shporer, J. C. Smith, J. H. Steffen, M. Still, G. Torres, J. Troeltzsch, J. D. Twicken, A. K. Uddin, J. E. Van Cleve, J. Voss, L. M. Weiss, W. F. Welsh, B. Wohler, K. A. Zamudio, The occurrence of rocky habitable-zone planets around solar-like stars from Kepler data. *Astron. J.* **161**, 36 (2020).
2. V. S. Airapetian, A. Glocer, G. V. Khazanov, R. O. P. Loyd, K. France, J. Sojka, W. C. Danchi, M. W. Liemohn, How hospitable are space weather affected habitable zones? The role of ion escape. *Astrophys. J.* **836**, L3 (2017).
3. C. Dong, M. Jin, M. Lingam, V. S. Airapetian, Y. Ma, B. van der Holst, Atmospheric escape from the TRAPPIST-1 planets and implications for habitability. *Proc. Natl. Acad. Sci. U.S.A.* **115**, 260–265 (2018).
4. Y. A. Yamashiki, H. Maehara, V. Airapetian, Y. Notsu, T. Sato, S. Notsu, R. Kuroki, K. Murashima, H. Sato, K. Namekata, T. Sasaki, T. B. Scott, H. Bando, S. Nashimoto, F. Takagi, C. Ling, D. Nogami, K. Shibata, Impact of stellar superflares on planetary habitability. *Astrophys. J.* **881**, 114 (2019).
5. V. S. Airapetian, R. Barnes, O. Cohen, G. A. Collinson, W. C. Danchi, C. F. Dong, A. D. Del Genio, K. France, K. Garcia-Sage, A. Glocer, N. Gopalswamy, J. L. Grenfell, G. Gronoff, M. Güdel, K. Herbst, W. G. Henning, C. H. Jackman, M. Jin, C. P. Johnstone, L. Kaltenegger, C. D. Kay, K. Kobayashi, W. Kuang, G. Li, B. J. Lynch, T. Lüftinger, J. G. Luhmann, H. Maehara, M. G. Mlynczak, Y. Notsu, R. M. Ramirez, S. Rugheimer, M. Scheucher, J. E. Schlieder, K. Shibata, C. Sousa-Silva, V. Stamenković, R. J. Strangeway, A. V. Usmanov, P. Vergados, O. P. Verkhoglyadova, A. A. Vidotto, M. Voytek, M. J. Way, G. P. Zank, Y. Yamashiki, Impact of space weather on climate and habitability of terrestrial-type exoplanets. *Int. J. Astrobiol.* **19**, 136–194 (2020).
6. C. P. Johnstone, Hydrodynamic escape of water vapor atmospheres near very active stars. *Astrophys. J.* **890**, 79 (2020).
7. D. V. Reames, in *Solar Energetic Particles. A Modern Primer on Understanding Sources, Acceleration and Propagation* (Springer, 2021), vol. 978.
8. N. Gopalswamy, S. Yashiro, Y. Liu, G. Michalek, A. Vourlidas, M. L. Kaiser, R. A. Howard, Coronal mass ejections and other extreme characteristics of the 2003 October–November solar eruptions. *J. Geophys. Res. Space Physics* **110**, A09S15 (2005).
9. G. P. Zank, W. K. M. Rice, C. C. Wu, Particle acceleration and coronal mass ejection driven shocks: A theoretical model. *J. Geophys. Res.* **105**, 25079–25095 (2000).
10. M. Desai, J. Giacalone, Large gradual solar energetic particle events. *Living Rev. Sol. Phys.* **13**, 3 (2016).
11. S. V. Poluianov, I. G. Usoskin, A. L. Mishev, M. A. Shea, D. F. Smart, GLE and Sub-GLE redefinition in the light of high-altitude polar neutron monitors. *Sol. Phys.* **292**, 176 (2017).
12. E. W. Cliver, H. Hayakawa, J. J. Love, D. F. Neidig, On the size of the flare associated with the solar proton event in 774 AD. *Astrophys. J.* **903**, 41 (2020).
13. F. Mekhaldi, J. R. McConnell, F. Adolphi, M. M. Arienzo, N. J. Chellman, O. J. Maselli, A. D. Moy, C. T. Plummer, M. Sigl, R. Muscheler, No coincident nitrate enhancement events in polar ice cores following the largest known solar storms. *J. Geophys. Res. Atmos.* **122**, 11,900–11,913 (2017).
14. F. Miyake, I. Usoskin, S. Poluianov, *Extreme Solar Particle Storms; The Hostile Sun* (IOP Publishing, 2019).
15. F. Miyake, I. P. Panyushkina, A. J. T. Jull, F. Adolphi, N. Brehm, S. Helama, K. Kanzawa, T. Moriya, R. Muscheler, K. Nicolussi, M. Oinonen, M. Salzer, M. Takeyama, F. Tokanai, L. Wacker, A single-year cosmic ray event at 5410 BCE registered in ^{14}C of tree rings. *Geophys. Res. Lett.* **48**, e93419 (2021).
16. N. Brehm, M. Christl, F. Adolphi, R. Muscheler, H.-A. Synal, F. Mekhaldi, C. Paleari, H.-H. Leuschner, A. Bayliss, K. Nicolussi, T. Pichler, C. Schlüchter, C. Pearson, M. Salzer, P. Fonti, D. Nievergelt, R. Hantemirov, D. Brown, I. Usoskin, L. Wacker, Tree rings reveal two strong solar proton events in 7176 and 5259 BCE. 10.21203/rs.3.rs-753272/v1 (2021).
17. F. Mekhaldi, R. Muscheler, F. Adolphi, A. Aldahan, J. Beer, J. R. McConnell, G. Possnert, M. Sigl, A. Svensson, H.-A. Synal, K. C. Welten, T. E. Woodruff, Multiradionuclide evidence for the solar origin of the cosmic-ray events of AD 774/5 and 993/4. *Nat. Commun.* **6**, 8611 (2015).
18. T. Sukhodolov, I. Usoskin, E. Rozanov, E. Asvestari, W. T. Ball, M. A. J. Curran, H. Fischer, G. Kovaltsov, F. Miyake, T. Peter, C. Plummer, W. Schmutz, M. Severi, R. Traversi, Atmospheric impacts of the strongest known solar particle storm of 775 AD. *Sci. Rep.* **7**, 45257 (2017).
19. I. G. Usoskin, S. A. Koldobskiy, G. A. Kovaltsov, E. V. Rozanov, T. V. Sukhodolov, A. L. Mishev, I. A. Mironova, Revisited reference solar proton event of 23 February 1956: Assessment of the cosmogenic-isotope method sensitivity to extreme solar events. *J. Geophys. Res. Space Physics* **125**, e2020JA027921 (2020).
20. M. Güdel, The sun through time. *Space Sci. Rev.* **216**, 143 (2020).
21. Y. Notsu, H. Maehara, S. Honda, S. L. Hawley, J. R. A. Davenport, K. Namekata, S. Notsu, K. Ikuta, D. Nogami, K. Shibata, Do Kepler superflare stars really include slowly rotating Sun-like stars?—Results using APO 3.5 m telescope spectroscopic observations and Gaia -DR2 Data. *Astrophys. J.* **876**, 58 (2019).
22. H. Maehara, T. Shibayama, S. Notsu, Y. Notsu, T. Nagao, S. Kusaba, S. Honda, D. Nogami, K. Shibata, Superflares on solar-type stars. *Nature* **485**, 478–481 (2012).
23. V. S. Airapetian, M. Jin, T. Lüftinger, S. B. Saikia, O. Kochukhov, M. Güdel, B. Van Der Holst, W. Manchester IV, One year in the life of young Suns: Data-constrained corona-wind model of κ^1 Ceti. *Astrophys. J.* **916**, 96 (2021).
24. K. Namekata, H. Maehara, S. Honda, Y. Notsu, S. Okamoto, J. Takahashi, M. Takayama, T. Ohshima, T. Saito, N. Katoh, M. Tozuka, K. L. Murata, F. Ogawa, M. Niwano, R. Adachi, M. Oeda, K. Shiraishi, K. Isogai, D. Seki, T. T. Ishii, K. Ichimoto, D. Nogami, K. Shibata, Probable detection of an eruptive filament from a superflare on a solar-type star. *Nat. Astron.* **6**, 241–248 (2022).
25. B. J. Lynch, V. S. Airapetian, C. R. DeVore, M. D. Kazachenko, T. Lüftinger, O. Kochukhov, L. Rosén, W. P. Abbett, Modeling a Carrington-scale stellar superflare and coronal mass ejection from κ^1*Cet*. *Astrophys. J.* **880**, 97 (2019).
26. J. D. Alvarado-Gómez, J. J. Drake, O. Cohen, S. P. Moschou, C. Garraffo, Suppression of coronal mass ejections in active stars by an overlying large-scale magnetic field: A numerical study. *Astrophys. J.* **862**, 93 (2018).
27. L. O'C Drury, An introduction to the theory of diffusive shock acceleration of energetic particles in tenuous plasmas. *Rep. Prog. Phys.* **46**, 973–1027 (1983).
28. W. K. M. Rice, G. P. Zank, G. Li, Particle acceleration and coronal mass ejection driven shocks: Shocks of arbitrary strength. *J. Geophys. Res. Space Physics* **108**, 1369 (2003).
29. J. Hu, G. Li, S. Fu, G. Zank, X. Ao, Modeling a single SEP event from multiple vantage points using the iPATH model. *Astrophys. J. Lett.* **854**, L19 (2018).
30. S. Fu, Y. Jiang, V. Airapetian, J. Hu, G. Li, G. Zank, Effect of star rotation rate on the characteristics of energetic particle events. *Astrophys. J. Lett.* **878**, L36 (2019).
31. G. Li, G. P. Zank, W. K. M. Rice, Energetic particle acceleration and transport at coronal mass ejection-driven shocks. *J. Geophys. Res. Space Physics* **108**, 1082 (2003).
32. G. Li, G. P. Zank, W. K. M. Rice, Acceleration and transport of heavy ions at coronal mass ejection-driven shocks. *J. Geophys. Res. Space Physics* **110**, A06104 (2005).
33. G. Li, A. Shalchi, X. Ao, G. Zank, O. P. Verkhoglyadova, Particle acceleration and transport at an oblique CME-driven shock. *Adv. Space Res.* **49**, 1067–1075 (2012).
34. J. Hu, G. Li, X. Ao, G. P. Zank, O. Verkhoglyadova, Modeling particle acceleration and transport at a 2D CME-driven shock. *J. Geophys. Res. Space Physics* **122**, 10,938–10,963 (2017).

35. D. V. Reames, L. M. Barbier, C. K. Ng, The spatial distribution of particles accelerated by coronal mass ejection-driven shocks. *Astrophys. J.* **466**, 473–486 (1996).
36. I. G. Richardson, T. T. von Rosenvinge, H. V. Cane, E. R. Christian, C. M. S. Cohen, A. W. Labrador, R. A. Leske, R. A. Mewaldt, M. E. Wiedenbeck, E. C. Stone, > 25 MeV proton events observed by the high energy telescopes on the STEREO A and B spacecraft and/or at Earth during the first ~ seven years of the STEREO mission. *Sol. Phys.* **289**, 3059–3107 (2014).
37. O. P. Verkhoglyadova, G. Li, G. P. Zank, Q. Hu, R. A. Mewaldt, Using the path code for modeling gradual SEP events in the inner heliosphere. *Astrophys. J.* **693**, 894–900 (2009).
38. O. P. Verkhoglyadova, G. Li, G. P. Zank, Q. Hu, C. M. S. Cohen, R. A. Mewaldt, G. M. Mason, D. K. Haggerty, T. T. von Rosenvinge, M. D. Looper, Understanding large SEP events with the PATH code: Modeling of the 13 December 2006 SEP event. *J. Geophys. Res. Space Physics* **115**, A12103 (2010).
39. Z.-Y. Ding, G. Li, J.-X. Hu, S. Fu, Modeling the 2017 September 10 solar energetic particle event using the iPATH model. *Res. Astron. Astrophys.* **20**, 145 (2020).
40. G. Li, M. Jin, Z. Ding, A. Bruno, G. A. de Nolfo, B. M. Randol, L. Mays, J. Ryan, D. Lario, Modeling the 2012 May 17 solar energetic particle event using the AWSoM and iPATH models. *Astrophys. J.* **919**, 146 (2021).
41. N. Gopalswamy, Chapter 2 - Extreme Solar Eruptions and their Space Weather Consequences, in *Extreme Events in Geospace*, N. Buzulukova, Ed. (Elsevier, 2018), pp. 37–63.
42. Z. Liu, L. Wang, R. F. Wimmer-Schweingruber, S. Krucker, G. M. Mason, Pan-spectrum fitting formula for suprathermal particles. *J. Geophys. Res. Space Physics* **125**, e28702 (2020).
43. M. Kretzschmar, The Sun as a star: Observations of white-light flares. *Astron. Astrophys.* **530**, A84 (2011).
44. M. J. Aschwanden, A. Caspi, C. M. S. Cohen, G. Holman, J. Jing, M. Kretzschmar, E. P. Kontar, J. M. McTiernan, R. A. Mewaldt, A. O'Flannagain, I. G. Richardson, D. Ryan, H. P. Warren, Y. Xu, Global energetics of solar flares. V. Energy closure in flares and coronal mass ejections. *Astrophys. J.* **836**, 17 (2017).
45. K. Namekata, T. Sakaue, K. Watanabe, A. Asai, H. Maehara, Y. Notsu, S. Notsu, S. Honda, T. T. Ishii, K. Ikuta, D. Nogami, K. Shibata, Statistical studies of solar white-light flares and comparisons with superflares on solar-type stars. *Astrophys. J.* **851**, 91 (2017).
46. T. Takahashi, Y. Mizuno, K. Shibata, Scaling relations in coronal mass ejections and energetic proton events associated with solar superflares. *Astrophys. J. Lett.* **833**, L8 (2016).
47. R. A. Mewaldt, M. D. Looper, C. M. Cohen, D. K. Haggerty, A. W. Labrador, R. A. Leske, G. M. Mason, J. E. Mazur, T. T. Von Rosenvinge, Energy spectra, composition, and other properties of ground-level events during solar cycle 23. *Space Sci. Rev.* **171**, 97–120 (2012).
48. O. Raukunen, R. Vainio, A. J. Tylka, W. F. Dietrich, P. Jiggens, D. Heynderickx, M. Dierckxsens, N. Crosby, U. Ganse, R. Siipola, Two solar proton fluence models based on ground level enhancement observations. *J. Space Weather Space Clim.* **8**, A04 (2018).
49. S. Koldobskiy, O. Raukunen, R. Vainio, G. A. Kovaltsov, I. Usoskin, New reconstruction of event-integrated spectra (spectral fluences) for major solar energetic particle events. *Astron. Astrophys.* **647**, A132 (2021).
50. A. Belov, H. Garcia, V. Kurt, H. Mavromichalaki, M. Gerontidou, Proton enhancements and their relation to the x-ray flares during the three last solar cycles. *Sol. Phys.* **229**, 135–159 (2005).
51. A. Youngblood, K. France, R. O. P. Loyd, A. Brown, J. P. Mason, P. C. Schneider, M. A. Tilley, Z. K. Berta-Thompson, A. Buccino, C. S. Froning, S. L. Hawley, J. Linsky, P. J. D. Mauas, S. Redfield, A. Kowalski, Y. Miguel, E. R. Newton, S. Rugheimer, A. Segura, A. Roberge, M. Vieytes, The MUSCLES treasury survey. IV. Scaling relations for ultraviolet, Ca II K, and energetic particle fluxes from M dwarfs. *Astrophys. J.* **843**, 31 (2017).
52. M. A. Tilley, A. Segura, V. Meadows, S. Hawley, J. Davenport, Modeling repeated M dwarf flaring at an Earth-like planet in the habitable zone: Atmospheric effects for an unmagnetized planet. *Astrobiology* **19**, 64–86 (2019).
53. V. S. Airapetian, A. Glocer, G. Gronoff, E. Hébrard, W. Danchi, Prebiotic chemistry and atmospheric warming of early Earth by an active young Sun. *Nat. Geosci.* **9**, 452–455 (2016).
54. C. H. Jackman, J. E. Frederick, R. S. Stolarski, Production of odd nitrogen in the stratosphere and mesosphere: An intercomparison of source strengths. *J. Geophys. Res. Oceans* **85**, 7495–7505 (1980).
55. V. S. Airapetian, C. H. Jackman, M. Mlynczak, W. Danchi, L. Hunt, Atmospheric beacons of life from exoplanets around G and K stars. *Sci. Rep.* **7**, 14141 (2017).
56. J. L. Grenfell, J. M. Grießmeier, P. Von Paris, A. B. C. Patzer, H. Lammer, B. Stracke, S. Gebauer, F. Schreier, H. Rauer, Response of atmospheric biomarkers to NOx-induced photochemistry generated by stellar cosmic rays for Earth-like planets in the habitable zone of M dwarf stars. *Astrobiology* **12**, 1109–1122 (2012).
57. B. H. Patel, C. Percivalle, D. J. Ritson, C. D. Duffy, J. D. Sutherland, Common origins of RNA, protein and lipid precursors in a cyanosulfidic protometabolism. *Nat. Chem.* **7**, 301–307 (2015).
58. M. Scheucher, K. Herbst, V. Schmidt, J. L. Grenfell, F. Schreier, S. Banjac, B. Heber, H. Rauer, M. Sinnhuber, Proxima Centauri b: A strong case for including cosmic-ray-induced chemistry in atmospheric biosignature studies. *Astrophys. J.* **893**, 12 (2020).
59. K. Kobayashi, in *Prebiotic Synthesis of Bioorganic Compounds by Simulation Experiments* (Springer Singapore, 2019), pp. 43–61.
60. P. B. Rimmer, S. Rugheimer, Hydrogen cyanide in nitrogen-rich atmospheres of rocky exoplanets. *Icarus* **329**, 124–131 (2019).
61. C. P. Johnstone, M. Bartel, M. Güdel, The active lives of stars: A complete description of the rotation and XUV evolution of F, G, K, and M dwarfs. *Astron. Astrophys.* **649**, A96 (2021).
62. D. Atri, Stellar proton event-induced surface radiation dose as a constraint on the habitability of terrestrial exoplanets. *Mon. Not. R. Astron. Soc. Lett.* **492**, L28–L33 (2020).
63. K. V. Getman, E. D. Feigelson, X-ray superflares from pre-main-sequence Stars: Flare energetics and frequency. *Astrophys. J.* **916**, 32 (2021).
64. C. Rab, M. Güdel, M. Padovani, I. Kamp, W. F. Thi, P. Woitke, G. Aresu, Stellar energetic particle ionization in protoplanetary disks around T Tauri stars. *Astron. Astrophys.* **603**, A96 (2017).
65. D. A. Clarke, A consistent method of characteristics for multidimensional magnetohydrodynamics. *Astrophys. J.* **457**, 291 (1996).

Acknowledgments

Funding: V.S.A. acknowledges support from the NASA/GSFC Sellers Exoplanet Environments Collaboration (SEEC), which is funded by the NASA Planetary Science Division's Internal Scientist Funding Model (ISFM), HST-XMM Newton Cycle 27, TESS Cycle 1, and NICER Cycle 2 programs. V.S.A. and G.L. acknowledge the International Space Science Institute and the supported International Team 464: The Role Of Solar And Stellar Energetic Particles On (Exo) Planetary Habitability (ETERNAL, http://issibern.ch/teams/exoeternal/) and support from ISFM "Energetic Particles in the Heliosphere and Magnetosphere" at NASA/GSFC. J.H. and G.L. acknowledge supports from NASA 80NSSC19K0075, 80NSSC19K0079, 80NSSC21K1836, 80NSSC20K1239, and 80NSSC21K1814. M.J. acknowledges support from NASA 80NSSC19K0774 and 80NSSC21K1782. We acknowledge the partial support of an NSF EPSCoR RII-Track-1 Cooperative Agreement OIA-1655280. **Author contributions**: V.S.A. was responsible for the initial concept, guided the modeling, and managed coauthor contributions to the paper. J.H. developed and executed the MHD/kinetic simulations. G.L. guided the modeling and participated in discussions on the scope of the work. J.H., V.S.A., G.L., and G.Z. contributed with analysis of model results. All authors contributed to the writing of the paper. **Competing interests**: The authors declare that they have no competing interests. **Data and materials availability**: All simulation data needed to evaluate the conclusions in the paper are published in Zenodo at https://doi.org/10.5281/zenodo.5842621.

Submitted 11 June 2021
Accepted 3 February 2022
Published 25 March 2022
10.1126/sciadv.abi9743

ScienceAdvances

Extreme energetic particle events by superflare-asssociated CMEs from solar-like stars

Junxiang HuVladimir S. AirapetianGang LiGary ZankMeng Jin

Sci. Adv., 8 (12), eabi9743. • DOI: 10.1126/sciadv.abi9743